BNL-96478-2011-JA

# *EVALUATION OF SURFACE FLUX PARAMETERIZATIONS WITH LONG-TERM ARM OBSERVATIONS*

Gang Liu[1, 2], Yangang Liu[1], and Satoshi Endo[1]

1 Brookhaven National Laboratory, Upton, NY 11973, USA
2 School of Atmospheric Sciences, Nanjing University, Nanjing 210093, China

Corresponding author: Gang Liu, School of Atmospheric Sciences, Nanjing University, Nanjing 210093 P. R. China, E-mail: gangliu@nju.edu.cn, TEL: +86-25-83595185 (office), FAX: +86-25-83593084

*Submitted to Monthly Weather Review*

**Atmospheric Sciences Division/Environmental Sciences Dept.**

**Brookhaven National Laboratory**

**U.S. Department of Energy**
**Office of Science**

Notice: This manuscript has been authored by employees of Brookhaven Science Associates, LLC under Contract No. DE-AC02-98CH10886 with the U.S. Department of Energy. The publisher by accepting the manuscript for publication acknowledges that the United States Government retains a non-exclusive, paid-up, irrevocable, world-wide license to publish or reproduce the published form of this manuscript, or allow others to do so, for United States Government purposes.

This preprint is intended for publication in a journal or proceedings. Since changes may be made before publication, it may not be cited or reproduced without the author's permission.

## DISCLAIMER

This report was prepared as an account of work sponsored by an agency of the United States Government. Neither the United States Government nor any agency thereof, nor any of their employees, nor any of their contractors, subcontractors, or their employees, makes any warranty, express or implied, or assumes any legal liability or responsibility for the accuracy, completeness, or any third party's use or the results of such use of any information, apparatus, product, or process disclosed, or represents that its use would not infringe privately owned rights. Reference herein to any specific commercial product, process, or service by trade name, trademark, manufacturer, or otherwise, does not necessarily constitute or imply its endorsement, recommendation, or favoring by the United States Government or any agency thereof or its contractors or subcontractors. The views and opinions of authors expressed herein do not necessarily state or reflect those of the United States Government or any agency thereof.

# Abstract

Surface momentum, sensible heat and latent heat fluxes are critical for atmospheric processes such as clouds and precipitation, and are parameterized in a variety of models ranging from cloud-resolving models to large scale weather and climate models. However, direct evaluation of the parameterization schemes for these surface fluxes is rare due to limited observations. This study takes advantage of the long-term observations of surface fluxes collected at the Southern Great Plains site by the Department of Energy Atmospheric Radiation Measurement program to evaluate the six surface flux parameterization schemes commonly used in the Weather Research and Forecasting (WRF) model and three US global climate models (GCMs). The unprecedented 7 year long measurements by the Eddy Correlation (EC) and Energy Balance Bowen Ratio (EBBR) methods permit statistical evaluation of all the six parameterizations under a variety of stability conditions and in the context of observational uncertainty. The results show that the momentum flux parameterization agrees best with the EC observations, and there are little differences among all the six schemes examined. For the sensible heat flux, the WRF-MM5 scheme performs best, while the WRF-Eta scheme worst. The three schemes for the latent heat flux used in the GCMs are relatively better compared to those used in the WRF model. Further analysis suggests that treatments of surface temperature and moisture availability may hold the key to improving parameterizations of sensible and latent heat fluxes, Bowen ratio, and evaporation fraction. The results are valuable for understanding and improving parameterization of surface turbulent fluxes in particular, and atmospheric boundary layer processes in general.



**Keywords**: surface flux; offline evaluation; observation; parameterization; surface layer

## 1. Introduction

Surface momentum, sensible heat and latent heat fluxes are critical for atmospheric processes such as clouds and precipitation formation, and are often parameterized in a variety of models due to limited grid resolution in these models, such as the Weather Research and Forecasting (WRF) model (Skamarock et al., 2008) and global climate models (GCMs). In numerical models, these turbulent flux parameterizations are collectively referred to the surface flux parameterization (SFP), and through SFP, the atmosphere are coupled with the underlying surface.

Evaluation of the SFP schemes is essential to any model development. There are generally two approaches for evaluating parameterizations: direct offline evaluation and full model online evaluation. Many studies on the SFP schemes have been conducted in an 'online' mode (e.g. Betts et al., 1997; Chen et al., 1997), whereby numerical models are run with different SFP schemes, and the impact of the SFP schemes on the simulation results of the numerical models are evaluated against observations. With the 'online' evaluation, the impact of the SFP schemes on the corresponding models can be investigated. The SFP schemes, however, themselves cannot be evaluated unambiguously with the online mode, since the parameterized turbulent fluxes are related to resolved meteorological quantities (wind speed, air temperature, humidity, and ground skin temperature), which are predicted by the numerical model rather than observed. The errors in the model-predicted quantities will in turn lead to errors in the parameterized turbulent fluxes.

The direct offline evaluation of the SFP schemes minimizes the compound errors associated with the full model evaluation, and is the focus of this paper. In the offline mode, the turbulent fluxes are calculated by the SFP schemes using the corresponding measurements of mean meteorological quantities as inputs, and the parameterized turbulent fluxes are evaluated against the concurrent measurements of surface turbulent fluxes. Direct offline SFP evaluation against observations is limited, due to lack of long-term and continuous flux observations in the surface layer. This has hindered proper assessment of the

SFP schemes and understanding of turbulent transfer between the atmosphere and the surface. The rare study by Cassano et al. (2001) evaluated seven SFP schemes, but was limited in several aspects by observations. Only 45 months of data collected in the Antarctica under stable stratification conditions with a temporal resolution of 1 h were used, and there were no comparisons for the latent heat flux.

The US Department of Energy (DOE) Atmospheric Radiation Measurement (ARM) program (www.arm.gov) has conducted continuous measurements of surface turbulent fluxes at the Southern Great Plains (SGP) site, by use of the Energy Balance Bowen Ratio (EBBR) stations since 1993, and by use of the Eddy Correlation (EC) stations since 1997. The EC method provides measurements of momentum, sensible heat and latent heat fluxes while the EBBR method only has the latter two. This study takes advantage of these long-term observations to evaluate the SFP schemes commonly used in the WRF model and in three major U.S. GCMs that participate in the FASTER project (www.bnl.gov/esm), e.g., Goddard Institute for Space Studies (GISS) GCM (Schmidt et al., 2006), Geophysical Fluid Dynamics Laboratory (GFDL) GCM (global atmosphere and land model, GFDL global atmospheric model development team, 2004) and National Center for Atmospheric Research (NCAR) GCM (Collins et al., 2004; NCAR Community Atmosphere Model, NCAR Technical Note, 2004).

The rest of the paper is organized as follows. The ARM SGP observations related to this study are described in Section 2, followed by the description of the evaluated SFP schemes in Section 3. The results from the six SFP schemes and comparisons with the observed surface fluxes are presented in Section 4. This study is summarized in Section 5.

## 2. Measurements related to this study

A primary objective of the ARM program is to improve scientific understanding of the fundamental physics related to interactions between clouds and radiative processes in the atmosphere, with emphasis on making continuous field measurements that enhance

evaluation and parameterization of cloud-related fast processes in climate models (Stokes and Schwartz, 1994; Ackerman and Stokes, 2003). The Southern Great Plains (SGP) site was the first field measurement site established by the ARM program, and the SGP central facility located near Lamont in north-central Oklahoma (36°36'18.0"N, 97°29'6.0"W, and 320 meters above sea level) houses the core instruments. Particularly useful to this paper are the EC and EBBR flux measurements.

The EC measurement system consists of a fast-response sonic anemometer for measuring three-dimensional winds and the speed of sound used to derive the air temperature, and an open-path infrared gas analyzer for the water vapor density and the $CO_2$ concentration. The eddy covariance technique is applied to the original measurements to derive 30-minute surface turbulent fluxes of momentum, sensible heat, latent heat, and carbon dioxide. The EBBR flux measurement system produces 30-minute estimates of the vertical fluxes of sensible and latent heat from measurements of net radiation, soil surface heat flux, and the vertical gradients of temperature and relative humidity.

Direct offline evaluation also needs the ground temperature as an input to the SFP schemes. At SGP, the ground temperature is measured with a downward pointing infrared thermometer (IRT) located at 10 m height above ground level. The IRT is a radiation pyrometer that measures the equivalent blackbody brightness temperature of the scene in its field of view, and provides a ground temperature every one minute. We aggregate the 1-min IRT measurements into the 30-min averages in consistency with the temporal resolution of the EC and EBBR flux measurements.

The period that has all the required coincident EC, EBBR and IRT measurements spans from 0000 September 12, 2003 to 2330 August 13, 2010 (UTC). This approximately 7 year of data are used in this study. To our knowledge, this data set is the longest that have been even analyzed so far, providing unprecedented statistics under a wide range of stability conditions. This is unique compared to previous studies.

## 3. Description of the surface flux parameterization schemes

### 3.1 General description

The sensible heat flux (SHF), latent heat flux (LHF) and momentum flux (MF) are respectively defined as follows:

$$\mathrm{SHF} = \rho \mathrm{C_p} \overline{w'\theta'}, \tag{1}$$

$$\mathrm{LHF} = \rho \mathrm{L_v} \overline{w'q'}, \tag{2}$$

$$\mathrm{MF} = -\rho \overline{u'w'} = \rho u_*^2, \tag{3}$$

where $\rho$ is the density of air; $\mathrm{C_p}$ is the specific heat of air at constant pressure; $\mathrm{L_v}$ is the latent heat of vaporization of water; $\theta$ is the potential temperature; $q$ is the specific humidity; $u$ and $w$ are horizontal and vertical wind speeds respectively; the prime denotes fluctuation from the average; $\overline{w'\theta'}$, $\overline{w'q'}$ and $-\overline{u'w'}$ are the kinematic definitions of the sensible heat flux, latent heat flux and momentum flux respectively; $u_*$ is the friction velocity. Note that Equation (3) is obtained when the coordinate system is aligned so that the *x*-axis points in the direction of the surface stress and the component $-\overline{v'w'}$ is thus eliminated.

In weather prediction and climate models, the standard approach to calculate a surface flux is expressing the surface flux as the difference of the corresponding mean quantity between the surface and the lowest model level assumed to be in the surface layer, and assuming the validity of the Monin-Obukhov Similarity Theory (MOST) (Monin and Obukhov, 1954). Mathematically, the equations in the kinematic forms are written as:

$$\overline{w'\theta'} = \mathrm{C_h} |U| (\theta_s - \theta), \tag{4}$$

$$\overline{w'q'} = \mathrm{C_q} |U| A_m (q_s - q), \tag{5}$$

$$u_*^2 = \mathrm{C_m} |U|^2, \tag{6}$$

$$\mathrm{C_h} = k^2 / \left\{ \left[ \ln\left(\frac{z}{z_0}\right) - \Psi_\mathrm{m}\left(\frac{z}{L}\right) + \Psi_\mathrm{m}\left(\frac{z_0}{L}\right) \right] \times \left[ \ln\left(\frac{z}{z_0}\right) - \Psi_\mathrm{h}\left(\frac{z}{L}\right) + \Psi_\mathrm{h}\left(\frac{z_0}{L}\right) \right] \right\}, \tag{7}$$

$$C_q = C_h, \tag{8}$$

$$C_m = k^2 / \left[ \ln\left(\frac{z}{z_0}\right) - \Psi_m\left(\frac{z}{L}\right) + \Psi_m\left(\frac{z_0}{L}\right) \right]^2, \tag{9}$$

$$|U|^2 = U^2 + V^2. \tag{10}$$

The notation in the equations follows the commonly used convention. Briefly, $|U|$ is the mean speed of the wind vector at the height $z$; $U$ and $V$ are the large-scale horizontal velocity components; $\theta_s$ is the potential temperature at the surface; $\theta$ is the potential temperature at the height $z$; $A_m$ is the moisture availability introduced as a measure of the degree of saturation at the ground (Zhang and Anthes, 1982); $q_s$ is the saturation specific humidity at the surface temperature; $q$ is the specific humidity at the height $z$; $C_{h,\,q,\,m}$ are the transfer coefficients for heat, moisture and momentum; $k$ is the Von Karman constant (assuming to be 0.4); $z$ is the reference height (i.e., in a weather/climate model, the height of the lowest model level; in experiments, the measurement height); $z_0$ is the roughness length; $L$ is the Monin-Obukhov length ($L = \dfrac{-u_*^3}{k\dfrac{g}{\theta_v}\overline{w'\theta_v'}}$, where $g/\overline{\theta_v}$ is the buoyancy parameter, $g$ is the gravity acceleration taken as 9.8 m s$^{-2}$, $\overline{\theta_v}$ is the mean virtual potential temperature, $\overline{w'\theta_v'}$ is the virtual potential temperature flux).

The potential temperature is calculated from $\theta = T\left(\dfrac{p_0}{p}\right)^{0.286}$, where $T$ is the air temperature, $p$ is the air pressure, $p_0$ is the reference pressure and set to be 100 kPa. The specific humidity is calculated from $q = \dfrac{r}{1+r}$, where $r$ is the mixing ratio. The surface potential temperature is given by $\theta_s = T_s\left(\dfrac{p_0}{p}\right)^{0.286}$, where $T_s$ is the ground skin temperature.

The saturation specific humidity $q_s$ is calculated from $q_s = 0.622\frac{e}{p_s}$, where $p_s$ is the surface air pressure and the saturation vapor pressure is given by $e = 0.6112\, e^{\left(17.67\times\frac{T_s - 273.16}{T_s - 29.66}\right)}$ (Stull, 1988).

The symbol $\Psi_{m,\,h}$ denote the stability profile function for momentum and heat (usually, the stability functions for heat and moisture are assumed to be the same). Various forms of the $\Psi_{m,\,h}$ function have been obtained (e.g. Businger et al., 1971; Dyer, 1974; Högström, 1988; Stull, 1988). As the SFP schemes use the same MOST theoretical framework, the differences lie mainly in their specification of the stability profile function and the various empirical parameters embedded in the different parameterizations.

In our offline evaluation, we use $T$, $p$, $r$, $U$ and $V$ measured by the EC flux measurement system with the sensors located at 3 m above ground level (i.e., $z$ is 3 m). The roughness length $z_0$ is set to 0.035 m (a characteristic value for the SGP Central Facility site), and $A_m$ is obtained by looking up a classification chart in the WRF model with the known land use type of the field where the observation site was located.

**3.2 The six SFP schemes examined**

The SFP schemes herein examined include three commonly used in the WRF model [the fifth-generation NCAR/Penn State Mesoscale Model (MM5), Eta Model (Eta) and Pleim-Xiu Land Surface Model (PX) schemes] (Skamarock et al., 2008), and those used in the three major US global climate models (GFDL, GISS and NCAR) (GFDL global atmospheric model development team, 2004; Schmidt et al., 2006 for GISS; Collins et al., 2004 for CAM). All the six schemes are based on the MOST theoretical framework, but with differences in their specific treatments of stability functions etc. Here their main characteristics are briefly introduced for purpose of comparison, with an emphasis on their differences.

### 3.2.1 WRF-MM5 scheme

The WRF-MM5 scheme uses the stability functions by Holtslag and De Bruin (1988) for stable conditions, and Paulson (1970) for unstable conditions. The Beljaars (1994) correction is applied to calculate the convective velocity scale, which is added to the horizontal wind speed in order to enhance the wind speed and prevent it from being zero under strong convection conditions. According to Zhang and Anthes (1982), depending on the sign and magnitude of the bulk Richardson number $R_b$, the stability regime is divided into four categories, on which either the turbulent fluxes are set to be zero or the forms of the stability profile functions $\Psi_{m,\,h}$ are determined. The atmospheric stability parameter $\frac{z}{L}$ is obtained by solving the relation between $\frac{z}{L}$ and $R_b$ iteratively (Beljaars and Holtslag, 1991).

### 3.2.2 WRF-Eta scheme

The WRF-Eta scheme is based on Janjic (1996). In this scheme, the effects of the viscous sub-layer are taken into account by introducing the roughness length for temperature and humidity (Zilitinkevich, 1995), which is different from that for momentum. The surface fluxes are calculated by an iterative method. Same as in the WRF-MM5 scheme, the Beljaars (1994) correction is also applied and the stability functions employ those by Holtslag and De Bruin (1988) and by Paulson (1970) for stable and unstable conditions respectively in this scheme.

### 3.2.3 WRF-PX scheme

The WRF-PX scheme was originally developed by Pleim (2006). It accounts for the difference in the sink/source heights of heat and momentum with parameterization of a viscous sub-layer in the form of a quasi-laminar boundary layer resistance. The stability functions are analytically estimated from large-scale state variables and are as follows:

(1) For stable conditions:

(I) When $0 < \frac{z}{L} < 1$, $\frac{z}{L} = \ln\left(\frac{z}{z_0}\right)\frac{\mathrm{R_b}}{1-\mathrm{R_b}/\mathrm{R_{crit}}}$, where $\mathrm{R_{crit}}$ is the critical Richardson number (0.25). $\Psi_{\mathrm{m,h}} = -\beta_{\mathrm{m,h}}\frac{z}{L}$, where $\beta_{\mathrm{m}} = \beta_{\mathrm{h}} = 1/\mathrm{R_{crit}}$.

(II) When $\frac{z}{L} > 1$, $\frac{z}{L} = \ln\left(\frac{z}{z_0}\right)\frac{\mathrm{R_b}}{1-\mathrm{R_{cut}}/\mathrm{R_{crit}}}$, where $\mathrm{R_{cut}} = \left[\ln\left(\frac{z}{z_0}\right) + \frac{1}{\mathrm{R_{crit}}}\right]^{-1}$.

$\Psi_{\mathrm{m,h}} = 1 - \beta_{\mathrm{m,h}} - \frac{z}{L}$.

(2) For unstable conditions:

$\Psi_{\mathrm{m,h}} = a_{\mathrm{m,h}}\ln\left\{1 - b_{\mathrm{m,h}}\left[\ln\left(\frac{z}{z_0}\right)\right]^{1/2}\mathrm{R_b}\right\}$, where $a_{\mathrm{m,h}} = c_{\mathrm{m,h}} + d_{\mathrm{m,h}}\ln\left[\ln\left(\frac{z}{z_0}\right)\right]$. Here these empirically determined constants are $b_{\mathrm{m}}$=13.0, $b_{\mathrm{h}}$=15.7, $c_{\mathrm{m}}$=0.031, $c_{\mathrm{h}}$=0.04, $d_{\mathrm{m}}$=0.276, $d_{\mathrm{h}}$=0.355.

### 3.2.4 CAM scheme

In the CAM scheme, the stability functions are based on Holtslag and De Bruin (1988) for stable conditions and on Paulson (1970) for unstable conditions. However, the stability functions based on Kader and Yaglom (1990) are employed for very unstable conditions and those based on Holtslag et al. (1990) are employed for very stable conditions, when atmospheric stratification and thermal effect are very strong.

The roughness lengths for momentum and heat (moisture) are estimated according to Zilitinkevich (1970) and Zeng and Dickinson (1998).The stability parameter $\frac{z}{L}$ is restricted to $-100 \le \frac{z}{L} \le 2$. The scalar wind speed is defined as

$$|U|^2 = U^2 + V^2 + U_c^2,$$

$$U_c = \begin{cases} 0.1\ \mathrm{ms}^{-1}, & \text{if } \dfrac{z}{L} \geq 0 \text{ (stable)} \\ \beta w_* = \beta \left( z_i \dfrac{g}{T} \overline{w'\theta_v'} \right)^{1/3}, & \text{if } \dfrac{z}{L} < 0 \text{ (unstable)} \end{cases}$$

Here $w_*$ is the convective velocity scale, and $\beta = 1$. $z_i$ is the convective boundary layer height, of which the value is taken as 1000 m.

### 3.2.5 GISS scheme

The GISS scheme (Schmidt et al., 2006) uses the stability functions of Holtslag and De Bruin (1988) and Paulson (1970) but with different empirical constants in the functions herein. The transfer coefficients for heat, moisture and momentum employ the forms by Hartke and Rind (1997). The roughness length for temperature over land is calculated according to Brutsaert (1982).

### 3.2.6 GFDL scheme

The GFDL scheme is virtually the same as the GISS scheme, except that different empirical constants are used in the stability functions of Holtslag and De Bruin (1988) and Paulson (1970).

For convenience, the major features of all the six SFP schemes evaluated are summarized in Table 1.

## 4. Results and analysis

### 4.1 Comparison of EBBR and EC measurements

As mentioned above, for sensible and latent heat fluxes, there are two independent sets of measurements from the EC and EBBR systems at the SGP site. In order to evaluate the SFP schemes in the context of observational uncertainty, we first compare the EBBR and EC observations. Figure 1 shows the sensible and latent heat fluxes from the EBBR and EC

observations in the form of occurring probability density. Generally, the two sets of observations are in good agreement with each other, with the correlation coefficients of 0.81 and 0.75, and the root mean square errors of 65.23 and 77.78 $Wm^{-2}$, respectively, for the sensible and latent heat fluxes. Similar findings were reported in previous studies (Brotzge and Crawford, 2003; Cook et al., 2006). Figure 1 (b) also shows that the EC system underestimated the latent heat flux compared to the EBBR system, which is consistent with the finding of Brotzge and Crawford (2003).

According to Brotzge and Crawford (2003) and Cook et al. (2006), one possible reason for the differences in the fluxes between the two systems is the theoretical assumption underlying the EBBR system that the eddy diffusivities of heat and water vapor are equal. Some studies have demonstrated that the two diffusivities are not equal under stable and neutral conditions. Another possible reason for the differences is that the sensors of the two systems are located at different heights, which induces differences in the fetch and/or flux footprints 'seen' by the instruments and creates differences in measurements. More work is needed to determine the exact reasons for the discrepancies, which is beyond the scope of this paper.

### 4.2 Comparison of parameterizations and observations

#### 4.2.1 Surface turbulent fluxes

Figure 2 compares the momentum flux (friction velocity) between the parameterizations and EC observations. It is evident that all the six SFP schemes perform well relative to the EC observations, with the correlation coefficients around 0.90 and the root mean square errors around 0.10 m $s^{-1}$. The differences between the different SFP schemes are small.

Figure 3 compares the sensible heat flux between the parameterizations and EC observations. Unlike the moment flux, all the schemes perform poorly, and underestimate the sensible heat flux compared to the EC observations when the observed EC fluxes are nonnegative. Relatively speaking, the WRF-MM5 scheme performs best with a correlation

coefficient of 0.55 and root mean square error of 125.91 W $m^{-2}$; the WRF-Eta scheme is the worst with a correlation coefficient of 0.36 and root mean square error of 145.31 W $m^{-2}$. The WRF-MM5 scheme does not significantly underestimate the sensible heat flux when the observed fluxes are close to zero under stable stratification conditions.

Similar to the sensible heat flux, all the schemes perform poorly for latent heat flux (Figure 4). When the observed latent heat fluxes are around zero under stable conditions, the WRF-Eta and WRF-PX schemes underestimate the latent heat flux significantly. Among the six schemes, the CAM scheme and the WRF-Eta scheme are the best and worst performers, respectively, with their corresponding correlation coefficients of 0.38 and 0.46 and root mean square errors of 85.82 and 74.94 W $m^{-2}$.

The parameterized sensible and latent heat fluxes are also compared to the EBBR observations, and the results show that they are similar to those in Figures 3 and 4. Briefly, the schemes underestimate the sensible heat flux when the observed fluxes are positive. Especially, the schemes underestimate the flux significantly when the observed counterparts are close to zero, except the WRF-MM5 scheme. The WRF-MM5 and WRF-Eta schemes are respectively the best and worst to reproduce the sensible heat flux based on their respective correlation coefficients to the observations, which are 0.60 and 0.42. Based on the correlation coefficient and root mean square error, the three schemes used in the GCM models produce better estimates for the latent heat flux than those used in the WRF model do, and the WRF-Eta and WRF-PX schemes underestimate the latent heat flux significantly when the observed values are approximately equal to zero. The WRF-Eta scheme underperforms compared to the other schemes based on its correlation coefficient to the observations, which is 0.52.

#### 4.2.2 Bowen ratio and evaporative fraction

It has been recognized that many processes are determined by the partition between sensible and latent heat fluxes. The two relative measures commonly used to gauge this partition are the Bowen ratio (Bowen, 1926) and evaporation fraction (Betts et al., 1997). The Bowen ratio

is defined as the ratio of the sensible heat flux to the latent heat flux; the evaporation fraction is defined as the ratio of the latent heat flux to the sum of the sensible and latent heat fluxes. Obviously, the Bowen ratio and evaporation fraction are inversely related to each other, but are preferred by different researchers in different communities. For example, Lu and Cai (2009) showed that the fractional change of the Bowen ratio with global warming approximately follows the rate expected from the Clausius-Clapeyron equation, and is closely related to the debate on global hydrological response to global warming. The two ratios are also essential to assess evapotranspiration.

In view of their importance, the six SFP schemes are also evaluated against the observations in terms of the Bowen ratio and evaporation fraction. Figure 5 compares the evaporative fraction between the six SFP schemes and EC observations. The data with $|\text{Latent Heat FLux} + \text{Sensible Heat Flux}| \geq 10\ \text{Wm}^{-2}$ are selected in the analysis to avoid unreasonably large values of the evaporative fraction. It is evident that all the schemes represent the evaporation ratio even worse than the corresponding sensible or latent heat flux. For the three schemes used in the WRF model, the correlation coefficients are as low as 0.11 and the root mean square errors as high as 1.10, while for the three schemes used in the GCM models, the corresponding quantities are respectively 0.09 and 1.17. Figure 6 compares the Bowen ratio between the parameterizations and EC observations. The data with $|\text{Latent Heat FLux}| \geq 10\ \text{Wm}^{-2}$ are selected in the analysis to avoid that the Bowen ratio becomes unreasonably too large. The results are similar to those of the evaporative fraction. For the three schemes used in the WRF model, the correlation coefficients are 0.10 and the root mean square errors around 4.9, while for the three schemes used in the GCM models, the corresponding quantities are respectively 0.09 and around 5.1.

The degradation of the parameterized evaporation fraction and Bowen ratio reveals possible magnification of the errors in the parameterized sensible and latent heat fluxes when converted into the respective ratios. This error magnification calls for a higher accuracy of

the SFP scheme, but none of the SFP schemes examined meet the conditions, and improvement is in order.

### 4.2.3 Analysis of Taylor diagram

The above analysis evaluates the performance of the six SFP schemes using the joint probability density function and in terms of the correlation coefficient and root mean square error. A more quantitative and complete picture of how well the parameterizations agree with observations can be obtained by use of the Taylor diagram (Taylor, 2001). The Taylor diagram compares three quantities — standard deviation, correlation coefficient, and centered root mean square difference — in a two-dimensional plot. The angle coordinate of the Taylor diagram gives the correlation between parameterization and observation; the radial coordinate compares the parameterized and observed amplitude of the variations as measured by standard deviation, and the distance between each parameterization point and the observed point gives the centered root mean square model error.

Figure 7 (a, b, c, d) shows the Taylor diagrams of the momentum flux (friction velocity), sensible and latent heat fluxes, and Bowen ratio for comparisons between the parameterizations and EC observations. Note that the EBBR observation is treated as a 'parameterization' in the diagrams for convenience of comparison. Shown in Figure 7 (a), all the schemes lie near the point marked 'observed', which suggests that all the six schemes parameterize the momentum flux very well compared to the EC observations. Moreover, the three schemes used in the GCMs have the best overall performance and their Taylor points almost overlap with one another. In Figure 7 (b), the WRF-MM5 scheme has the shortest distance to the EC observation among all the schemes, which suggests it has the least centered RMS error against the observations. Moreover, its standard deviation is closest to that of the observed, indicating the variations of its parameterization are of the correct amplitude, and it also has the largest correlation coefficient among all the schemes. Thus the WRF-MM5 scheme is the best to parameterize the sensible heat flux compared to the EC

observations, while the WRF-Eta scheme is the worst, which has the largest distance to the observed and the least correlation coefficient. In Figure 7 (c), the three schemes used in the GCMs have the largest correlation coefficients and the most correct standard deviations, thus have the least centered RMS errors against the EC observations (the shortest distances to the observed), which suggests they are relatively better to parameterize the latent heat flux. Comparatively, the three schemes used in the WRF model are worse. In Figure 7 (d), the points of the six schemes are almost overlapped with one another, with all of them having low correlation coefficients with the EC observations and standard deviations much less than that of the EC observations. This result confirms the proceeding finding that all the six schemes poorly quantify the Bowen ratio or evaporation fraction.

#### 4.2.4 Analysis of relative Euclidean distance

Although the Taylor diagram allows a visual comparison of three important quantities (correlation coefficient, standard deviation and centered root mean square error), it ignores the mean bias, another crucial quantity in assessing any parameterizations. Furthermore, different schemes may have different performances for different quantities, and different quantities have different units. Therefore, it is desirable to have a single metric that can measure the overall performance of a parameterization and allows for comparing parameterizations for different quantities. For this purpose, here we introduce a new metric — relative Euclidean distance D, which is defined as:

$$\mathrm{D} = \sqrt{\left(\frac{\bar{x}-\bar{y}}{\bar{y}}\right)^2 + \left(\frac{\sigma_x-\sigma_y}{\sigma_y}\right)^2 + \left(c_{xy}-1\right)^2},$$

where $x$ and $y$ are respectively the model and observation data, $\bar{x}$, $\bar{y}$, $\sigma_x$, $\sigma_y$ are the corresponding mean values and standard deviations, $c_{xy}$ is the correlation coefficient between $x$ and $y$. Evidently, the value of D equals to 0 for a perfect match, and increases as the agreement degrades.

Figure 8 compares the relative Euclidean distances of the momentum, sensible and latent heat fluxes and the Bowen ratio for the six SFP schemes. The EC measurements are used as the reference and the EBBR observation is again treated as a 'parameterization' here for convenience of comparison. In terms of the relative Euclidean distance, the momentum flux is reproduced best, and all the six schemes perform very well. The sensible heat flux is reproduced worst, and the performances of the six schemes are not greatly different from one another except the WRF-PX scheme is relatively the worst among the six schemes. The latent heat flux is reproduced better than the sensible heat flux, and the WRF-PX scheme is the worst on this quantity. The three schemes used in the GCM models reproduce the latent heat flux better than the three schemes used in the WRF model do, which is in coincidence with the aforementioned conclusion. The Bowen ratio is reproduced better than the sensible heat flux is, but worse than the latent heat flux is, and the relative Euclidean distances for the six schemes are almost the same as each other, which suggests all the schemes are not reproducing the Bowen ratio very well. The probable reason that causes the nearly constant D value of the Bowen ratio for all the schemes is that to avoid unreasonably large values of the Bowen ratio, the data with the magnitude of the observed latent heat flux < 10 W $m^{-2}$, or when the stratification is relatively stable or neutral, have been removed in the analysis. The elimination of these data points reduces the D value of the Bowen ratio and the differences between the different schemes. All the data are used in the analysis of the sensible and latent heat fluxes. It is also interesting to note that for the latent heat flux, the EBBR measurement is no better than all the SFP schemes except the PX scheme, suggesting the need for improving measurements as well. For convenience, Table 2 summarizes the values used to generate Figure 8.

**4.3 Effect of atmospheric stability**

In Figures 2 ~ 4, it is found that the discrepancies between the parameterizations and observations are related to the values of the observed fluxes. It has been known that the sign

and magnitude of surface turbulent fluxes are closely associated with the atmospheric stability, which has diurnal and seasonal variations (Stull, 1988). Atmospheric stability conditions play a major role in the tendency for energy and materials to move vertically through the surface layer to the free atmosphere. In an unstable atmosphere, vertical motion is enhanced and turbulent fluxes are enhanced. In a stable atmosphere, vertical motion is suppressed and turbulent fluxes are more likely to be reduced. The stability functions in the transfer coefficients of all the six schemes are derived from the MOST, and the differences mainly lie in their specification of the stability function and the various empirical parameters embedded in the functions. As the MOST estimates turbulent exchanges for scalar and momentum fluxes and describes the relationship between the turbulent statistical quantities and the mean meteorological quantities in the surface layer, a MOST-based parameterization is expected to be closely related to the atmospheric stability.

In order to investigate the effect of the atmospheric stability on the performances of the SFP schemes, the comparisons between the parameterizations and observations are shown in terms of atmospheric stability classifications. In this study, the atmospheric stability is divided into 13 classifications according to the values of the atmospheric stability parameter ($\frac{z}{L}$), which span from less than -5 to larger than 5. The classifications are divided equally between -5 and 5, except that the values between -0.01 and 0.01 are set as a classification which represents the near-neutral conditions. Figure 9 is the frequency distribution of the atmospheric stability parameter, showing that the atmospheric stability is dominantly under the weak unstable, near-neutral and weak stable conditions that are within the range of -1 and 1, for most of the observations.

Figure 10 compares the mean relative errors of the parameterizations as a function of the atmospheric stability. The mean relative error is calculated as the averaged value of $(x\text{-}y)/y$ within an atmospheric stability classification, where $x$ is the parameterized value, $y$ is the corresponding observed EC value. A negative (positive) value of relative difference indicates

an underestimation (overestimation) by the parameterization compared to the observation when the observed value is positive. For convenience of comparison, the EBBR observation is here treated as a 'parameterization'. Figure 10 (a) shows that all the SFP schemes somewhat overestimate the momentum flux compared to the observations, and they display the same error pattern of increasing when the atmosphere becomes more unstable or more stable, with a minimum near the neutral atmosphere. Different schemes perform differently under different conditions of atmospheric stability. The WRF-MM5 scheme has the least errors under unstable conditions, while the WRF-Eta scheme has the largest errors under stable conditions. But, the differences between the six schemes are not significant in general. Figure 10 (b) shows that the SFP schemes underestimate the sensible heat flux under unstable conditions, with the underestimation increases with instability. Note that all the schemes also underestimate the sensible heat flux under stable conditions since the observed sensible heat fluxes are negative under those conditions. The WRF-MM5 scheme exhibits the best performance with the least mean relative errors under most of atmospheric stability conditions, while the WRF-Eta scheme does worst, especially under moderate stable conditions. It is also shown that the EBBR observations underestimate the sensible heat flux compared to the EC observations under stable conditions. As shown in Figure 10 (c), the SFP schemes overestimate the latent heat flux under strongly unstable conditions. When the stability increases, the schemes appear to underestimate the flux. However, except the WRF-Eta scheme, they overestimate the flux under stable conditions since the observed fluxes are negative under stable conditions. As for the sensible heat flux, the WRF-Eta scheme suffers from the largest mean relative errors under most of atmospheric stability conditions, especially under moderately stable conditions. Also, the EBBR observations overestimate the latent heat flux compared to the EC observations mainly under stable conditions. Figure 10 (d) compares the results for the Bowen ratio. Evidently, all the SFP schemes underestimate the Bowen ratio, and also they almost overlap with one another, which is consistent with what in Figure 7 (d) and Figure 8, while the EBBR observation overestimates it. Although the relative

errors for the six schemes under unstable conditions are not large, there appears a steep increase when the stability parameter approaches zero. It is noteworthy that only the data with $|\text{Latent Heat FLux}| \geq 10$ Wm$^{-2}$ are shown here to avoid unreasonably large values of the Bowen ratio, which literally removes the data with the stability parameter larger than 1. Nevertheless, based on the results for the sensible and latent heat fluxes in Fig 10 (b) and (c), the relative errors are likely very large when the stability parameter is larger than one.

**5. Summary and discussion**

The long-term (2003-2010) observations of surface momentum, sensible heat and latent heat fluxes collected with the EC and EBBR systems at the Southern Great Plains site by the Department of Energy Atmospheric Radiation Measurement program are used to evaluate the six surface flux parameterization schemes commonly used in the Weather Research and Forecasting (WRF) model and three U.S. global climate models (GFDL, GISS and NCAR). The schemes are assessed in terms of their performances in quantifying correlation coefficient, variability as measured by standard deviation, centered root mean square error, and mean bias using an integrative analysis of joint occurrence frequency, Taylor diagram, and the newly introduced relative Euclidean distance. The effect of atmospheric stability on the parameterization schemes is also examined.

It is shown that the sensible and latent heat fluxes observed by the EBBR and EC systems are in reasonably good agreement with each other. However, the discrepancy is still noteworthy. Possible reasons were given by Brotzge and Crawford (2003) and Cook et al. (2006). However, more work is needed to determine the exact reasons for these differences.

The momentum flux is parameterized best compared to the other fluxes. For the momentum flux, the parameterizations are very close to the EC observations based on the correlation coefficients and small root mean square errors. All the six SFP schemes perform well, and there are negligible differences between the different schemes. All the SFP schemes

slightly underestimate the sensible heat flux compared to the EC observations when the observed EC fluxes are nonnegative. The WRF-MM5 scheme performs best, while the WRF-Eta scheme does worst. Compared with the EC-observed latent heat flux, the WRF-Eta scheme performs worst and the CAM scheme best based on the correlation coefficient between the parameterizations and observations.

The SFP schemes underestimate the sensible heat flux when the EBBR-observed fluxes are positive. The WRF-MM5 and WRF-Eta schemes are respectively the best and worst based on their respective correlation coefficients to the observations. Overall the three schemes used in the GCM models produce better estimates for the latent heat flux than those used in the WRF model do, compared to the EBBR observations. The WRF-Eta scheme underperforms compared to the other schemes based on its correlation coefficient to the observations.

All the schemes are relatively poor to reproduce the evaporation fraction and Bowen ratio, which reveals that the errors in the parameterized sensible and latent heat fluxes are magnified. The magnification of the errors in the parameterized sensible and latent heat fluxes when converted into the respective ratios presents higher accuracy requirement for the SFP scheme, but none of the SFP schemes examined are satisfactory in this regard.

Dependence of the SFP schemes on the atmospheric stability are further examined, and the following results are obtained: First, the error between the EC-observed momentum flux and the parameterized counterparts reaches the minimum near neutral conditions, and becomes increasingly larger when the atmospheric stratification becomes stronger (more stable or more unstable). Second, compared to the EC observations, the WRF-MM5 scheme has the best performance to parameterize the sensible heat flux as it has the least mean relative errors under most of atmospheric stability conditions, while the WRF-Eta scheme does the worst, especially it performs significantly worse than the other schemes under stable conditions. Third, the SFP schemes tend to overestimate the latent heat flux under strongly unstable conditions as well as stable conditions. Fourth, even though the data under strongly

stable and neutral stratification conditions are removed to avoid unreasonably large values of the Bowen ratio, the Bowen ratio is reproduced by all the schemes badly, and the differences between the different schemes are small. Finally, the EBBR observations underestimate the sensible heat flux and overestimate the latent heat flux under stable conditions compared to the EC observations, which is consistent with the findings of Brotzge and Crawford (2003), wherein they found that the EC system often overestimated the sensible heat flux and underestimated the latent heat flux under stable conditions compared to the EBBR system.

In general, the parameterized fluxes are not very different from one another, indicating the parameterizations are not very sensitive to the stability functions and empirical constants used in the SFP schemes examined here. Further parameterization improvement requires examining the common MOST theoretical framework itself. The study also suggests that the MOST works relatively better under convective and neutral conditions than under stable conditions. The SFP schemes under stable conditions warrant special attention.

Another possible reason for the poor performance in sensible and latent heat flux parameterizations lies in the accuracy of observed surface temperature and moisture availability. According to Zhan et al. (1996), errors in predicted sensible heat fluxes are predominantly sensitive to errors in air and surface temperatures. A 10% error in surface temperature (°C) can result in over 50% error in predicted sensible heat flux. This explains why the parameterizations of the momentum flux are in relatively better agreement with the observations, since surface and air temperatures are not required for the parameterizations of the momentum flux. The surface temperature is also needed to determine the surface specific humidity in the SFP schemes. The other key parameter that affects the latent heat flux is the moisture availability. It is expected that the poor parameterizations of sensible and latent flux will have serious effects on model simulations. The requirement for more accurate specification of surface temperature and moisture availability poses additional challenges to the online model evaluation, which we plan to do next.

**Acknowledgment:**

This work is part of the FASTER project (www.bnl.gov/esm) supported by the DOE Earth System Modeling (ESM) Program. The first author is partly funded by National Basic Research Program of China (973 Program) under Grant No. 2010CB428501 for the work.

**References:**

Ackerman, T. P., and G. M. Stokes, 2003: The atmospheric radiation measurement program. *Phys. Today*, S-0031-9228-0301-030-5, 38–44.

Beljaars, A. C. M., and A. A. M. Holtslag, 1991: On flux parameterization over land surfaces for atmospheric models. *J. Appl. Meteor.*, **30**, 327–341.

Beljaars, A. C. M., 1994: The parameterization of surface fluxes in large-scale models under free convection, *Q. J. R. Meteorol. Soc.*, **121**, 255–270.

Betts, A., F. Chen, K. Mitchell, and Z. Janjic, 1997: Assessment of the land surface and boundary layer models in two operational versions of the NCEP Eta model using FIFE data. *Mon. Wea. Rev.*, **125**, 2896–2916.

Bowen, I. S., 1926: The ratio of heat losses by conduction and by evaporation from any water surface. *Phys. Rev.*, **27**, 779–787.

Brotzge, J. A., and K. C. Crawford, 2003: Examination of the surface energy budget: a comparison of eddy correlation and Bowen ratio measurement systems. *J. Hydrometeorol.*, **4**, 160–178.

Brutsaert, W. H., 1982: *Evaporation into the Atmosphere: Theory, History and Applications*. D. Reidel, Norwell, Massachusetts, 299 pp.

Businger, J. A., J. C. Wyngaard, Y. Izumi, and E. F. Bradley, 1971: Flux-profile relationships in the atmospheric surface layer. *J. Atmos. Sci.*, **28**, 181–189.

Cassano, J. J., T. R. Parish, and J. C. King, 2001: Evaluation of turbulent surface flux parameterizations for the stable surface layer over Halley, Antarctica. *Mon. Wea. Rev.*, **129**, 26–46.

Chen, F., Z. Janjic, and K. Mitchell, 1997: Impact of atmospheric surface-layer parameterizations in the new land-surface scheme of the NCEP mesoscale Eta model. *Boundary-Layer Meteorol.*, **85**, 391–421.

Collins, W. D., P. J. Rasch, and Others, 2004: Description of the NCAR Community Atmosphere Model (CAM 3.0). Technical Report NCAR/TN-464+STR, National Center for Atmospheric Research, Boulder, Colorado, 210 pp.

Cook, D. R., D. J. Holdridge, and M. L. Fischer, 2006: Comparison of ECOR, EBBR, and CO2FLX4m system fluxes. *Sixteenth ARM Science Team Meeting Proceedings*, Albuquerque, NM, March 27–31, 2006.

Dyer, A. J., 1974: A review of flux-profile relationships. *Boundary-Layer Meteorol.*, **7**, 363–372.

GAMDT (The GFDL Global Atmospheric Model Development Team), 2004: The new GFDL global atmosphere and land model AM2–LM2: evaluation with prescribed SST simulations. *J. Climate*, **17**, 4641–4673.

GAMDT (The GFDL Global Atmospheric Model Development Team): The Monin-Obukhov module for FMS. Available online at http://data1.gfdl.noaa.gov/~arl/pubrel/m/am2/exp/fv/path_names.html.

Hartke, G. J., and D. Rind, 1997: Improved surface and boundary layer models for the Goddard Institute for Space Studies general circulation model. *J. Geophys. Res.*, **102**, 16407–16422.

Högström, U., 1988: Non-dimensional wind and temperature profiles in the atmospheric surface layer: A re-evaluation. *Boundary-Layer Meteorol.*, **42**, 55–78.

Holtslag, A. A. M., and H. A. R. De Bruin, 1988: Applied modeling of the nighttime surface energy balance over land. *J. Appl. Meteorol.*, **27**, 689–704.

Holtslag, A. A. M., E. I. F. De Bruijn, and H.-L. Pan, 1990: A high-resolution air mass transformation model for short range weather forecasting. *Mon. Wea. Rev.*, **118**, 1561–1575.

Janjic, Z. I., 1996: The surface layer in the NCEP Eta Model. *Eleventh Conference on Numerical Weather Prediction*, Norfolk, VA, 19–23 August, American Meteorological Society, Boston, MA, 354–355.

Kader, B. A., and A. M. Yaglom, 1990: Mean fields and fluctuation moments in unstably stratified turbulent boundary layers. *J. Fluid Mech.*, **212**, 637–662.

Lu, J., and M. Cai, 2009: Stabilization of the atmospheric boundary layer and the muted global hydrological cycle response to global warming. *J. Hydrometeorol.*, **10**, 347–353.

Monin, A. S., and A. M. Obukhov, 1954: Basic laws of turbulent mixing in the atmosphere near the ground. *Akad. Nauk. S. S. S. R. Trud. Gefiz. Inst. Tr.*, **24**, 163–187.

NCAR (National Center for Atmospheric Research): NCAR/TN-464+STR, NCAR Technical Note, June 2004

Paulson, C. A., 1970: The mathematical representation of wind speed and temperature profiles in the unstable atmospheric surface layer. *J. Appl. Meteorol.*, **9**, 857–861.

Pleim, J. E., 2006: A simple, efficient solution of flux–profile relationships in the atmospheric surface layer. *J. Appl. Meteorol. Climatol.*, **45**, 341–347.

Schmidt, G. A., R. Ruedy, and Others, 2006: Present-day atmospheric simulations using GISS Model E: Comparison to in situ, satellite, and reanalysis data. *J. Climate*, **19**, 153–192.

Skamarock, W. C., J. B. Klemp, J. Dudhia, D. O. Gill, D. M. Barker, M. G. Duda, X. Y. Huang, W. Wang, and J. G. Powers, 2008: A description of the advanced research WRF version 3. NCAR Tech Note NCAR/TN-475+STR, 113 pp. PDF text available at http://www.mmm.ucar.edu/wrf/users/docs/arw_v3.pdf.

Stokes, G. M., and S. E. Schwartz, 1994: The Atmospheric Radiation Measurement (ARM) program: Programmatic background and design of the cloud and radiation test bed. *Bull. Am. Meteorol. Soc.*, **75**, 1201–1221.

Stull, R. B., 1988: *An introduction to boundary layer meteorology*. Kluwer Academic Publishers, 666 pp.

Taylor, K. E., 2001: Summarizing multiple aspects of model performance in a single diagram. *J. Geophys. Res.*, **106**, 7183–7192.

Zeng, X., and R. E. Dickinson, 1998: Effect of surface sublayer on surface skin temperature and fluxes. *J. Climate*, **11**, 537–550.

Zhan, X., W. Kustas, and K. Humes, 1996: An intercomparison study on models of sensible heat flux over partial canopy surfaces with remotely sensed surface temperature. *Remote Sens. Environ.*, **S8**, 242–256.

Zhang, D.-L., and R. A. Anthes, 1982: A high-resolution model of the planetary boundary layer—Sensitivity tests and comparisons with SESAME-79 data. *J. Appl. Meteorol.*, **21**, 1594–1609.

Zilitinkevich, S. S., 1970: *Dynamics of the Atmospheric Boundary Layer*. Leningrad Gidrometeor, 291 pp.

Zilitinkevich, S. S., 1995: Non-local turbulent transport: pollution dispersion aspects of coherent structure of convective flows. *Air Pollution III — Volume I. Air Pollution Theory and Simulation*, Eds. H. Power, N. Moussiopoulos and C.A. Brebbia. Computational Mechanics Publications, Southampton Boston, 53–60.

Table 1. Major features and distinctions of the six SFP schemes evaluated

| SFP scheme | Outline of major features and distinctions |
|---|---|
| WRF-MM5 | • The Beljaars (1994) correction is applied to calculate the convective velocity scale<br>• Stability functions:<br>Holtslag and De Bruin (1988) for stable conditions<br>Paulson (1970) for unstable conditions |
| WRF-Eta | • The effects of the viscous sub-layer are taken into account by introducing the roughness length for temperature and humidity (Zilitinkevich, 1995)<br>• The Beljaars (1994) correction is also applied to calculate the convective velocity scale under free convection conditions<br>• The stability functions are based on Paulson (1970) and Holtslag and De Bruin (1988) |
| WRF-PX | • Accounting for the difference in the sink/source heights of heat and momentum with parameterization of a viscous sub-layer<br>• The surface layer similarity functions are analytically estimated from large-scale state variables |
| CAM | • The roughness lengths for momentum and heat are based on Zilitinkevich (1970)<br>• The scalar wind speed is defined as $\|U\|^2 = U^2 + V^2 + U_c^2$,<br>$U_c = \begin{cases} 0.1\ \mathrm{ms}^{-1}, & \text{if } \frac{z}{L} \geq 0 \text{ (stable)} \\ \beta w_* = \beta\left(z_i \frac{g}{T}\overline{w'\theta_v'}\right)^{1/3}, & \text{if } \frac{z}{L} < 0 \text{ (unstable)} \end{cases}$ |
| GISS | • The roughness length for temperature over land is based on Brutsaert (1982)<br>• The stability functions of Paulson (1970) and Holtslag and De Bruin (1988) are used, but with different constants in the functions |
| GFDL | • Completely the same as the GISS scheme, except with the different empirical constants in the stability functions of Paulson (1970) and Holtslag and De Bruin (1988) |

Table 2. Summary of relative Euclidean distance (D), mean value (M), standard deviation (S) and correlation coefficient (C).

| Observations / Schemes | | Momentum flux | Sensible heat flux | Latent heat flux | Bowen ratio |
|---|---|---|---|---|---|
| EC | D | 0 | 0 | 0 | 0 |
| | M | 0.310 | 39.527 | 41.541 | 1.759 |
| | S | 0.180 | 109.089 | 63.364 | 4.011 |
| | C | 1 | 1 | 1 | 1 |
| EBBR | D | N/A | 0.189 | 0.927 | 0.928 |
| | M | N/A | 39.462 | 63.641 | 0.900 |
| | S | N/A | 104.923 | 108.673 | 2.213 |
| | C | N/A | 0.815 | 0.745 | 0.351 |
| WRF-MM5 | D | 0.282 | 1.830 | 0.905 | 1.353 |
| | M | 0.321 | -30.538 | 43.478 | 0.062 |
| | S | 0.226 | 110.582 | 107.201 | 2.768 |
| | C | 0.890 | 0.547 | 0.418 | 0.103 |
| WRF-Eta | D | 0.309 | 1.886 | 0.792 | 1.354 |
| | M | 0.346 | -30.560 | 26.764 | 0.060 |
| | S | 0.224 | 115.812 | 85.264 | 2.766 |
| | C | 0.858 | 0.361 | 0.383 | 0.103 |
| WRF-PX | D | 0.262 | 2.159 | 1.097 | 1.354 |
| | M | 0.339 | -42.533 | 47.928 | 0.065 |
| | S | 0.219 | 142.438 | 122.198 | 2.701 |
| | C | 0.890 | 0.495 | 0.437 | 0.106 |
| CAM | D | 0.283 | 1.775 | 0.621 | 1.354 |
| | M | 0.360 | -27.169 | 33.074 | 0.061 |
| | S | 0.219 | 101.094 | 78.114 | 2.756 |
| | C | 0.915 | 0.455 | 0.462 | 0.104 |
| GISS | D | 0.264 | 1.854 | 0.663 | 1.354 |
| | M | 0.348 | -30.638 | 36.474 | 0.063 |
| | S | 0.219 | 104.774 | 85.443 | 2.724 |
| | C | 0.913 | 0.467 | 0.450 | 0.105 |
| GFDL | D | 0.260 | 1.840 | 0.644 | 1.354 |
| | M | 0.346 | -30.027 | 34.898 | 0.063 |
| | S | 0.219 | 101.838 | 81.986 | 2.729 |
| | C | 0.913 | 0.465 | 0.450 | 0.105 |

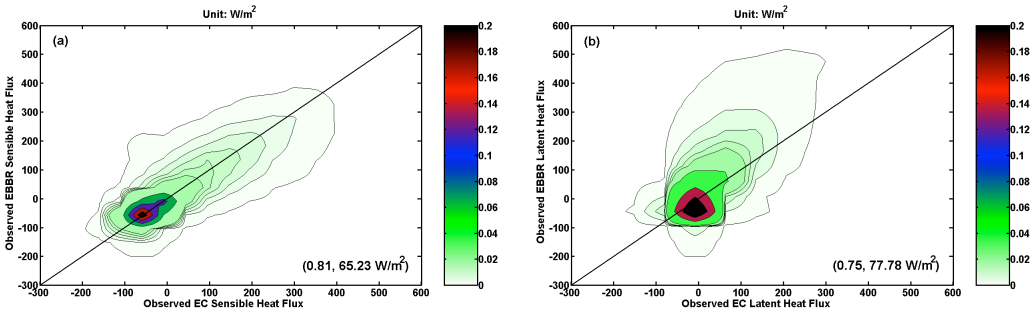


Figure 1 Comparison of the surface (a) sensible heat and (b) latent heat fluxes between the EBBR and EC observations in the form of occurring probability density. The bracketed numbers on each plot are the correlation coefficient and the root mean square error between the two sets of observations, respectively.

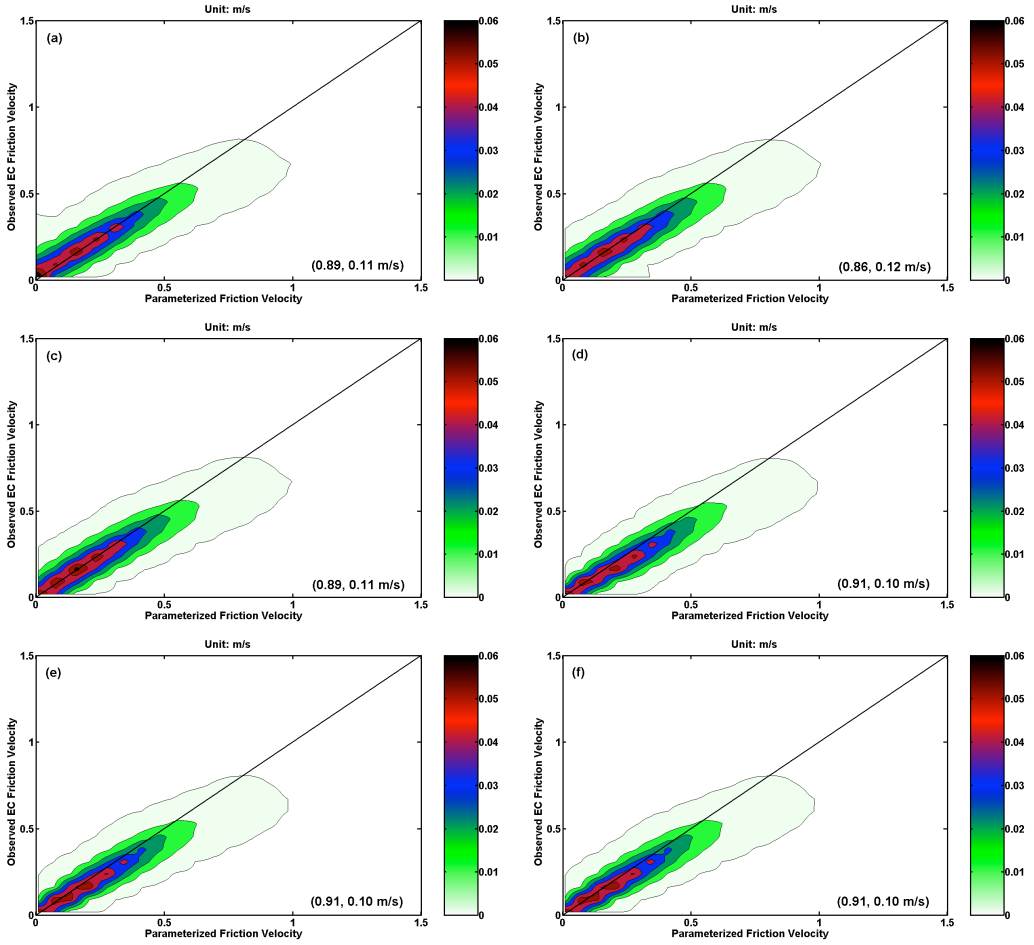


Figure 2 Comparison of the momentum flux (friction velocity) between the parameterizations and EC observations: (a) WRF-MM5 vs. EC, (b) WRF-Eta vs. EC, (c) WRF-PX vs. EC, (d) CAM vs. EC, (e) GISS vs. EC, (f) GFDL vs. EC. The bracketed numbers on each plot are the correlation coefficient and the root mean square error, respectively.

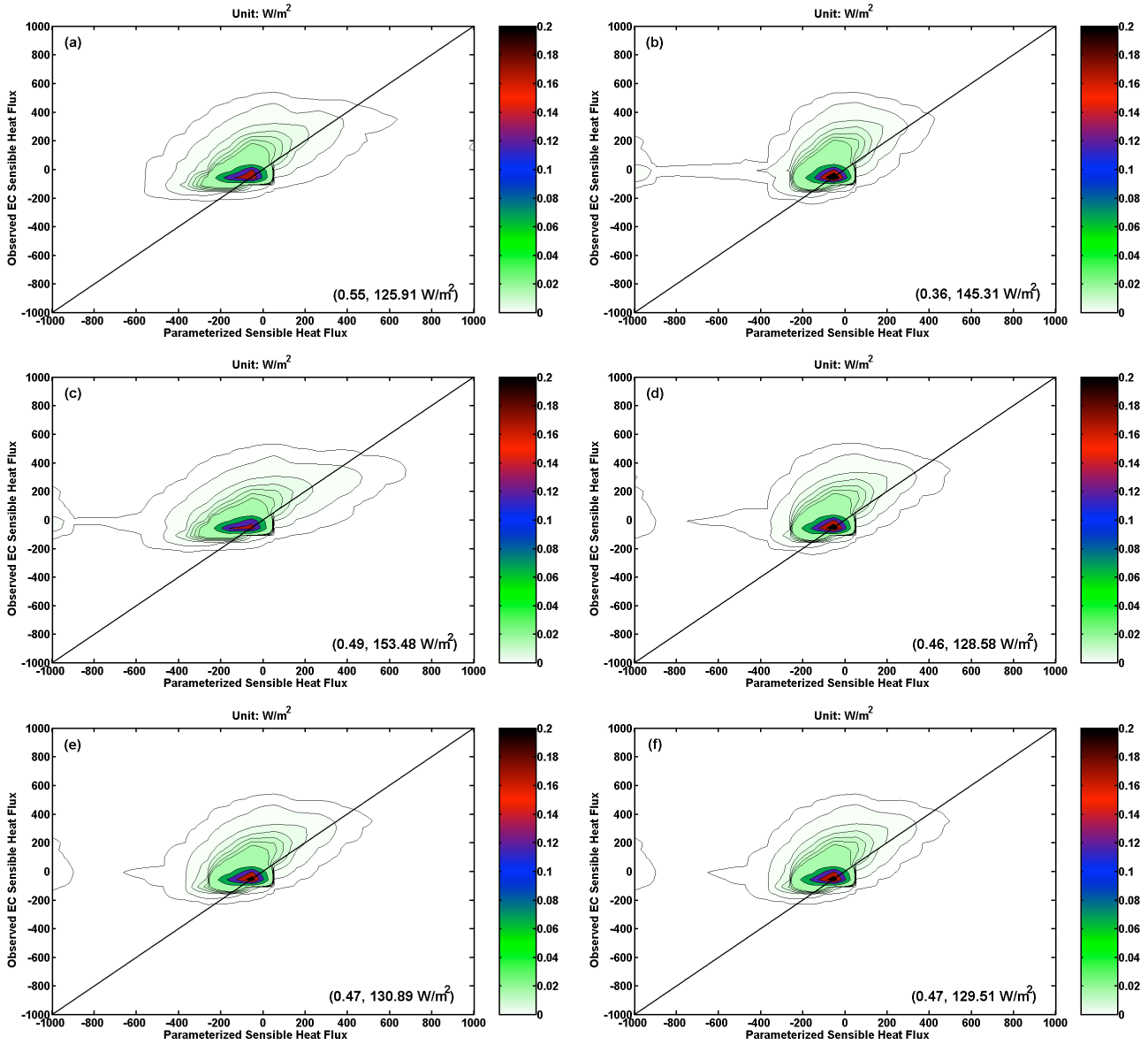


Figure 3 Comparison of the sensible heat flux between the parameterizations and EC observations: (a) WRF-MM5 vs. EC, (b) WRF-Eta vs. EC, (c) WRF-PX vs. EC, (d) CAM vs. EC, (e) GISS vs. EC, (f) GFDL vs. EC. The bracketed numbers on each plot are the correlation coefficient and the root mean square error, respectively.

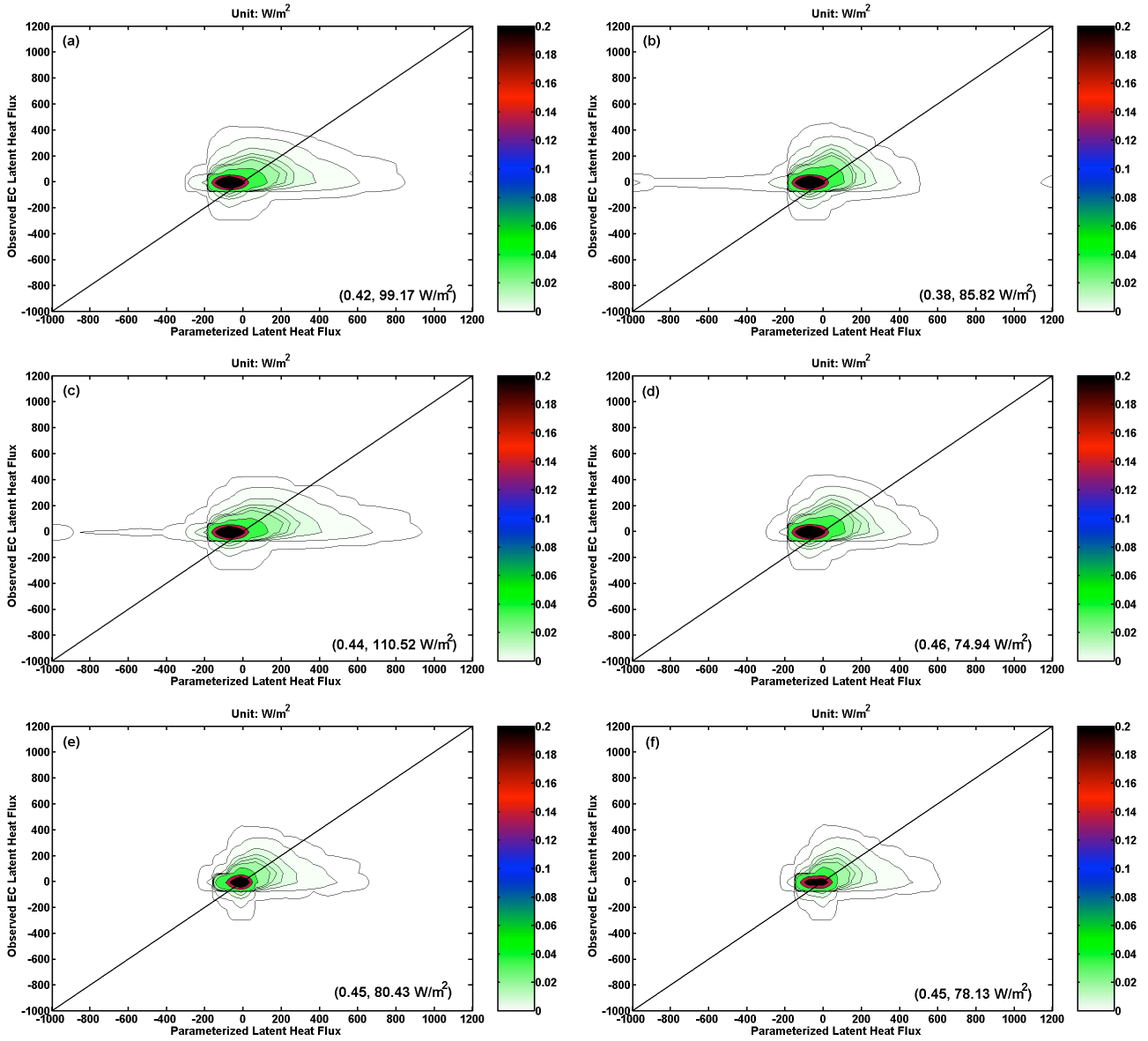


Figure 4 Comparison of the latent heat flux between the parameterizations and EC observations: (a) WRF-MM5 vs. EC, (b) WRF-Eta vs. EC, (c) WRF-PX vs. EC, (d) CAM vs. EC, (e) GISS vs. EC, (f) GFDL vs. EC. The bracketed numbers on each plot are the correlation coefficient and the root mean square error, respectively.

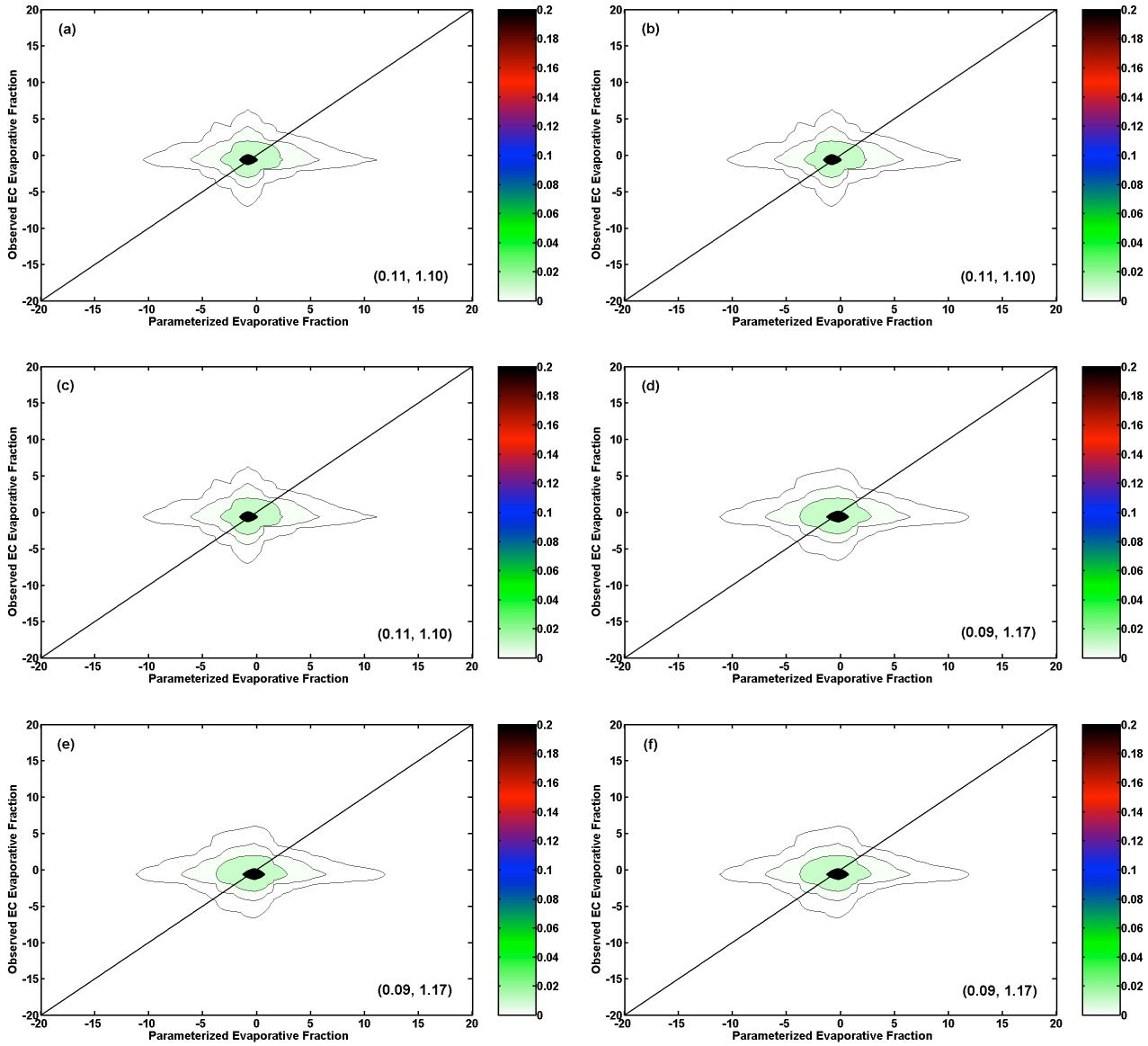


Figure 5 Comparison of the evaporative fraction between the parameterizations and EC observations: (a) WRF-MM5 vs. EC, (b) WRF-Eta vs. EC, (c) WRF-PX vs. EC, (d) CAM vs. EC, (e) GISS vs. EC, (f) GFDL vs. EC. The bracketed numbers on each plot are the correlation coefficient and the root mean square error, respectively.

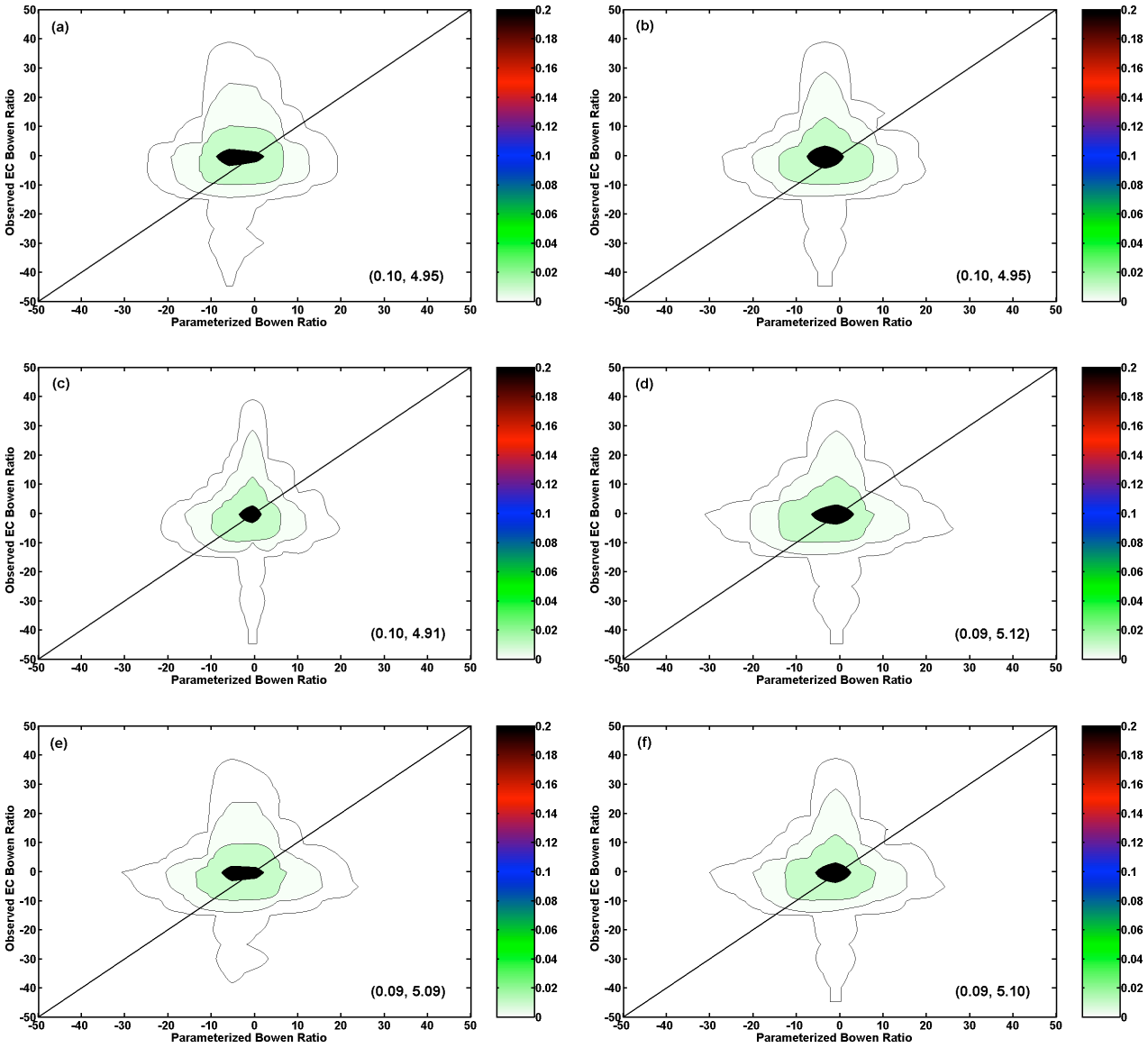


Figure 6 Comparison of the Bowen ratio between the parameterizations and EC observations: (a) WRF-MM5 vs. EC, (b) WRF-Eta vs. EC, (c) WRF-PX vs. EC, (d) CAM vs. EC, (e) GISS vs. EC, (f) GFDL vs. EC. The bracketed numbers on each plot are the correlation coefficient and the root mean square error, respectively.

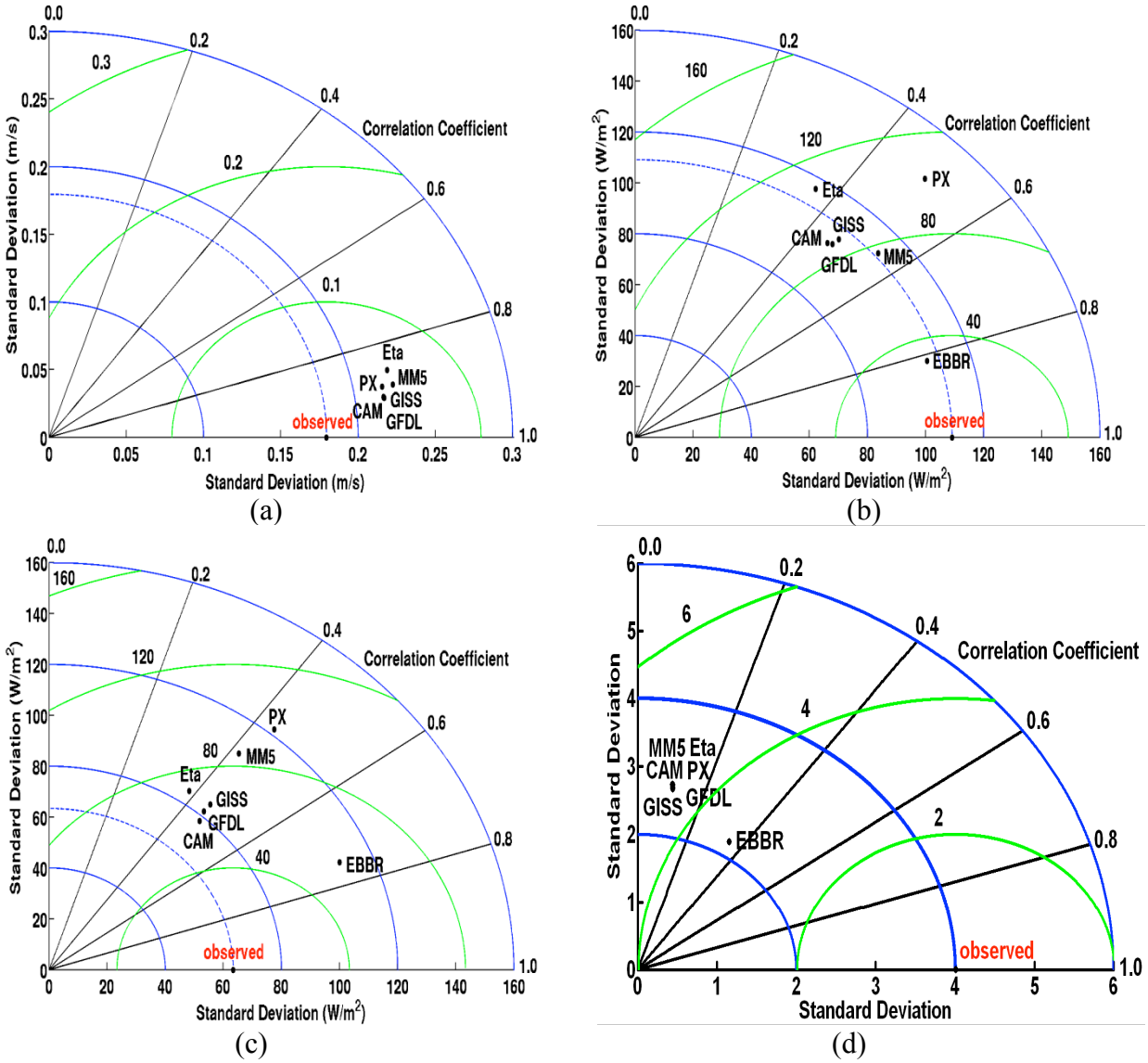


Figure 7 Taylor diagrams of (a) the momentum flux (friction velocity), (b) the sensible heat flux, (c) the latent heat flux and (d) the Bowen ratio for comparisons between the parameterizations and EC observations. For convenience of comparison, the EBBR observation is treated as a 'parameterization' here. Blue arc represents the standard deviation of parameterization and observation, while green arc represents the centered root mean square difference between parameterization and observation.

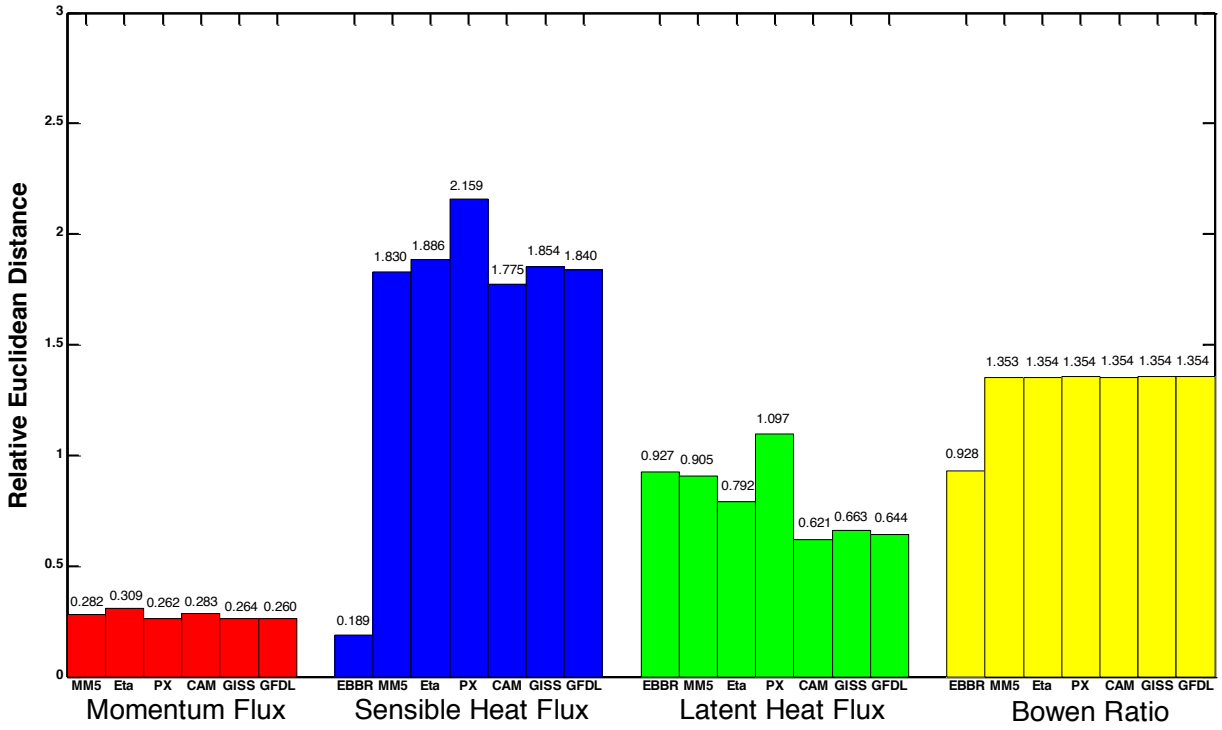


Figure 8 Relative Euclidean distances of the momentum, sensible and latent heat fluxes and the Bowen ratio for comparisons between the parameterizations and EC observations. For convenience of comparison, the EBBR observation is treated as a 'parameterization' here.

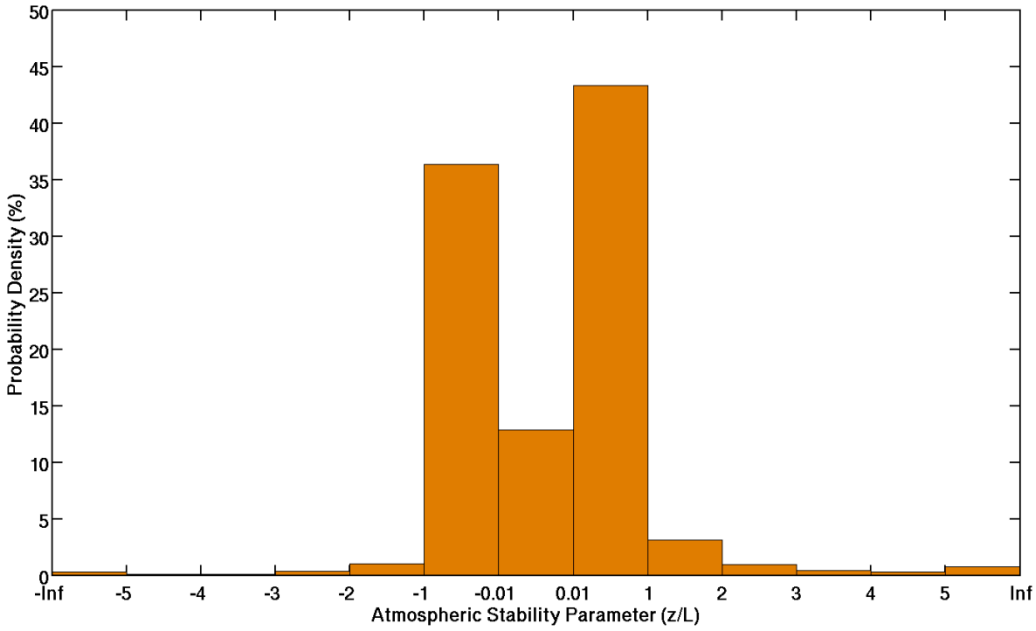


Figure 9 Frequency distribution of the atmospheric stability parameter.

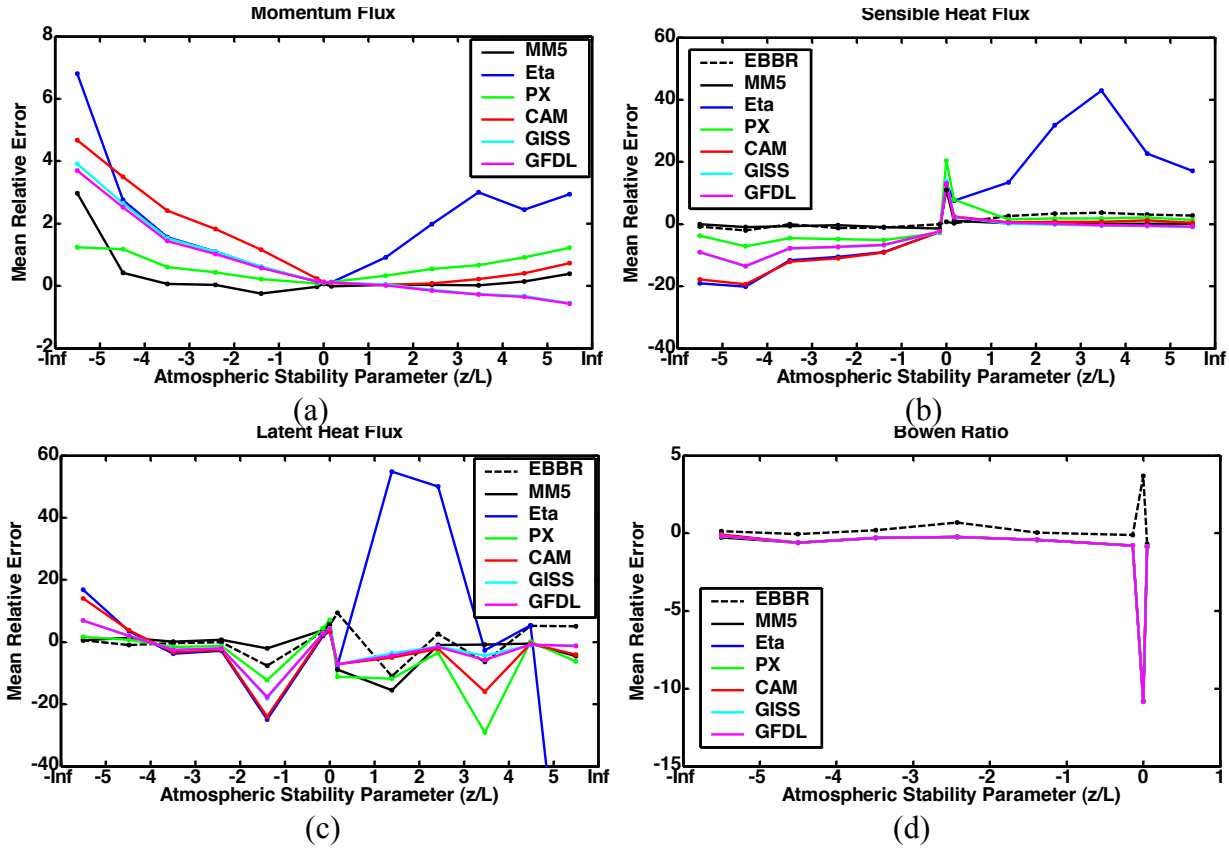


Figure 10 Comparison of (a) the momentum flux, (b) the sensible heat flux, (c) the latent heat flux and (d) the Bowen ratio between the parameterizations and EC observations in the form of the mean relative error varying with the atmospheric stability. See the text for the definition of the mean relative error shown in the fractional error on each plot. For convenience of comparison, the EBBR observation is treated as a 'parameterization' here.